


## Vibrational dynamics of extreme $2 \times 2$ and $3 \times 3$ potassium iodide nanowires encapsulated in single-walled carbon nanotubes

Victor G. Ivanov,<sup>1,\*</sup> Nataliya Kalashnyk,<sup>2,†</sup> Jeremy Sloan,<sup>3,‡</sup> and Eric Faulques<sup>2,§</sup>

<sup>1</sup>*Faculty of Physics, Sofia University, 5 James Bourchier Boulevard, 1164 Sofia, Bulgaria*

<sup>2</sup>*Institut des Matériaux Jean Rouxel (IMN), Université de Nantes, CNRS, 2 rue de la Houssinière, Boîte Postale 32229, 44322 Nantes Cedex 3, France*

<sup>3</sup>*Department of Physics, University of Warwick, Gibbett Hill Road, Coventry CV4 7AL, United Kingdom*

 (Received 23 March 2018; revised manuscript received 9 August 2018; published 28 September 2018)

We study the normal vibrations of  $2 \times 2$  and  $3 \times 3$  potassium iodide (KI) crystalline nanowires embedded in single-walled carbon nanotubes (SWCNTs) by density functional theory calculations, accompanied by Raman spectroscopy measurements on SCWNTs infiltrated with KI. The calculated stand-alone KI nanowires are found to be fully stable, while their vibrational energies are very close to the additional low-frequency Raman lines experimentally detected in the KI@SCWNT systems and ascribed to the encapsulated KI crystals. The difference between the relaxed and observed geometries of the KI nanowires evidences an electron transfer from these nanowires to the surrounding SWCNTs. Calculated radial and tangential vibrational frequencies of KI nanowires compared to those of supplementary discovered Raman lines suggest that the nanowire-SWCNT interaction is of a van der Waals origin and exclude the possibility of functionalization between the KI nanocrystals and the nanotube walls.

DOI: [10.1103/PhysRevB.98.125429](https://doi.org/10.1103/PhysRevB.98.125429)

### I. INTRODUCTION

An underlying paradigm in nanoscience is that the confinement of matter to lower spatial dimensions results in a variety of new properties not attainable in the bulk. In this context the low-dimensional carbon allotropes, fullerenes (zero-dimensional), carbon nanotubes [CNTs; one-dimensional (1D)], and graphene (two-dimensional), are among the most widely studied materials in the last two decades. In particular, quantum wires made of filled single-walled or double-walled carbon nanotubes (SWCNTs or DWCNTs) have an important place amid these nanomaterials. The encapsulated material may either be functionalized with the inner CNT wall by forming covalent bonds [1] or may crystallize into metastable stand-alone 1D crystals, which are stabilized by van der Waals interactions with the surrounding CNT [2–5]. In both cases, charge transfer between the CNT and the filler results in *p*- or *n*-type doping, modifying the host tubule band structure [6–8]. The microstructure of such materials can be investigated by transmission electron microscopy (TEM) [1–5,9–11] or scanning transmission electron microscopy [12].

Recent research is indicating many new possibilities for producing modified or even completely novel electronic and optoelectronic properties from SWCNT embedded nanocrystals, also known as extreme nanowires (ENs), as a result of forming them in a confining geometry. ENs of alkali halides,

metallic chalcogenides, and monoatomic elemental chains encapsulated in SWCNTs have been widely reported [3,9,11–13]. These materials can display novel hybridization, as in the case of embedded CuBr@SWCNT [1], embedded conductivity in one-dimensional chains of sulfur in S@SWCNT [11], and charge-density waves in iodine chains embedded in DWCNTs [11]. A decade ago, Sceats *et al.* performed a thorough study of the electronic structure of 1D KI crystals embedded in SWCNTs predicting a charge transfer dependent on the SWCNT diameter [14]. Further new possibilities are inferred by theoretical considerations, which indicate that atomic chains, helices, and ENs of pure Te [15] and binary SnTe [16] should lead to the direct observation of Peierls distortions. These works also demonstrate the potentiation of thermoelectric characteristics in the ENs induced by nanostructuring, exceeding *ZT* in the bulk by a factor of 12 or more.

In many interesting studies, Raman spectroscopy has been utilized for successfully probing several CNT composite systems, like SnTe@SWCNT [1], KI@SWCNT [17], HgTe@DWCNT [18], and S@SWCNT [11]. Typically, these works report on small-frequency upshifts and modification of the spectral form of the radial breathing mode (RBM) and *G* modes of the surrounding CNT upon filling. The observed spectral changes scale with the evolution of the CNT Raman bands upon electrochemical doping and have been ascribed to charge transfer between the filler material and the CNT [8], although strain-induced frequency shifts could also play a significant role [17]. Therefore, spectral modifications reported in these examples are intrinsic to the encapsulating CNT and do not indicate the detection of vibrational eigenmodes of the encapsulated nanowires themselves.

Recently, the latter issue was addressed by Spencer *et al.* [19], who established a sharp electronic resonance for a

\*vgi@phys.uni-sofia.bg

†Present address: GeePs, CNRS UMR 8507 – CentraleSupélec – UPSud – UPMC, 11 rue Joliot Curie, 91192 Gif sur Yvette, France; n.kalashnyk@yahoo.com

‡j.sloan@warwick.ac.uk

§eric.faulques@cnrs-immn.fr

( $2 \times 2$ )-atom per cross section HgTe@SWCNT nanowire at an excitation energy of 1.76 eV. Under resonant excitation several intrinsic modes of the 1D HgTe crystal, which possesses unique structural and electronic properties, emerge in the Raman spectrum. The supporting density functional theory (DFT) calculations allowed us to assign the most intense Raman line to a RBM-like mode of the nanowire, in which the Hg and Te atoms vibrate in phase in radial directions relative to the nanowire axis.

As mentioned above, alkali halides are very prone to 1D crystallization in CNT. However, contrary to metallic chalcogenides, the fourfold atomic coordination in the  $2 \times 2$  alkali halide nanowires is closely related to the corresponding bulk forms with nearly cubic arrangement of cations and anions, together with Coulomb interactions [4,5]. Therefore, such confined systems are very motivating since one may expect that the pattern of normal vibrations of the alkali halide nanowires is not equivalent to that of metal chalcogenide nanowires for similar sizes and therefore induces different electronic interactions with the surrounding CNT.

The intrinsic vibrational dynamics of alkali halide nanowires does not yet seem to be addressed in the literature, either theoretically or experimentally. This motivates us to fill this gap by focusing on the following issues. (i) We study theoretically by means of DFT calculations the equilibrium structure, the stability, the  $\Gamma$ -point normal vibrations, and the lattice phonons of stand-alone KI nanowires with a small,  $2 \times 2$  and  $3 \times 3$ , cross section. While interaction between the filler material and the surrounding nanotube can be anticipated *a priori*, the stand-alone calculations give a good first-approximation picture of the frequency spectrum and the atomic displacement pattern of the nanowire [19]. This approach could be justified *a posteriori* by the fact that the calculated normal frequencies of the nanowire do not overlap significantly with the phonon spectrum of the surrounding CNT; that is, the mode mixing between the filler and the CNT is expected to be small. (ii) We report on detailed Raman spectroscopy studies of KI@SWCNT at several wavelengths, which allows us to identify the intrinsic vibrational modes of the encapsulated KI material. The correspondence between the calculated and experimental Raman frequencies is discussed, and implications for the nanowire-CNT interactions are inferred.

## II. EXPERIMENTAL METHODS AND CALCULATION DETAILS

Commercial SWCNTs from NanoIntegris PureTubes (96% and 99% pure, 1.2–1.7 nm diameter, 300 nm to  $5 \mu\text{m}$  length) were infiltrated with KI using a melt infiltration protocol described previously [2]. We used two different SWCNT grades of purity as a cross-check that the new spectral features emerging upon KI infiltration originate from the filler material and are not related to impurities. Briefly, the SWCNTs were washed, dissolved in *N*-methyl-2-pyrrolidone (NMP), dried, and preheated to 1173 K to remove solvent and to open the tubes. The prepared SWCNTs were afterwards ground with highly pure KI (99.99%, Aldrich) in a glove box, then transferred to a quartz capillary. This mixture was preheated at 673 K for 20 min; then the vial was sealed under vacuum and

heated for 37 h with a plateau at 1054 K during 24 h and left to cool down to room temperature. High-resolution transmission electron microscopy (HRTEM) images show that 40% to 50% of SWCNTs were filled by KI with  $2 \times 2$  and  $3 \times 3$  one-dimensional KI crystals (the composite are hereafter referred to as KI@SWCNT).

HRTEM experiments were carried out with a JEM-ARM 200F microscope operating at 80 kV equipped with a CEOS aberration corrector and a Gatan SC1000 ORIUS camera with a  $4008 \times 2672$  pixel charge-coupled device. Dispersions of KI@SWCNT were drop cast onto 3.05-mm Cu specimen support grids (Agar Scientific) prior to HRTEM investigations.

Micro-Raman experiments were performed with Horiba Jobin-Yvon T64000 and LabRam spectrometers in triple subtractive and single monochromator mode with diffraction grating of 1800 and 600 grooves/mm, respectively. Four laser excitations,  $\lambda_{\text{exc}} = 458$  and 514 nm (Ar<sup>+</sup> laser), 532 nm (diode laser), and 633 nm (He-Ne laser) with respective energies at 2.71, 2.41, 2.33, and 1.96 eV, were provided by Ar<sup>+</sup>, diode, and helium-neon lasers, respectively. Spectra were collected at room temperature in the range between 30 and  $3000 \text{ cm}^{-1}$ , allowing us to register the spectra of the filling and carbon nanotubes. The diameter of the laser spot on the sample surface was about  $2 \mu\text{m}$  for the fully focused laser beam with  $50\times$  objective magnification. The KI@SWCNT samples were generally found to be homogeneous under a microscope without extraneous KI microcrystalline residues. Raman instruments were calibrated against the Stokes Raman signal of pure Si at  $520.5 \text{ cm}^{-1}$  using a silicon wafer. The spectral resolution was  $2 \text{ cm}^{-1}$ . In each experiment, several spectra were recorded at different spots in the samples.

The calculations were performed with the QUANTUM ESPRESSO DFT plane-wave code [20] by making use of the generalized gradient approximation with the Perdew-Burke-Ernzerhof functional [21] and norm-conserving pseudopotentials for the core electrons. The plane-wave energy cutoff was set at 500 eV (36.7 Ry). The self-consistent calculations for the 1D nanowire were performed on a  $1 \times 1 \times 4$  Monkhorst-Pack (MP) *k*-point mesh. We assessed the chosen DFT scheme by performing test calculations for the bulk potassium iodide on a  $4 \times 4 \times 4$  MP grid. The optimized K-I distance was obtained at  $3.5307 \text{ \AA}$ , which deviates by less than 0.4% from the experimental value of  $3.532 \text{ \AA}$ .

## III. CALCULATION PREDICTIONS FOR STAND-ALONE $2 \times 2$ AND $3 \times 3$ KI NANOWIRES

This section is devoted to the calculation and analysis of 1D KI nanowires starting from the bulk KI parameters. The final relaxed structures are given, and the phonons are calculated after geometry optimization. The  $\Gamma$ -point modes are classified with their different symmetries and sorted by frequencies.

### A. Equilibrium geometry

The starting geometries of the two nanowires were chosen to be those of infinite rods along the [001] direction of a bulk KI crystal with  $2 \times 2$  and  $3 \times 3$  cross sections. The initial K-I distance was set equal to the corresponding bulk value of

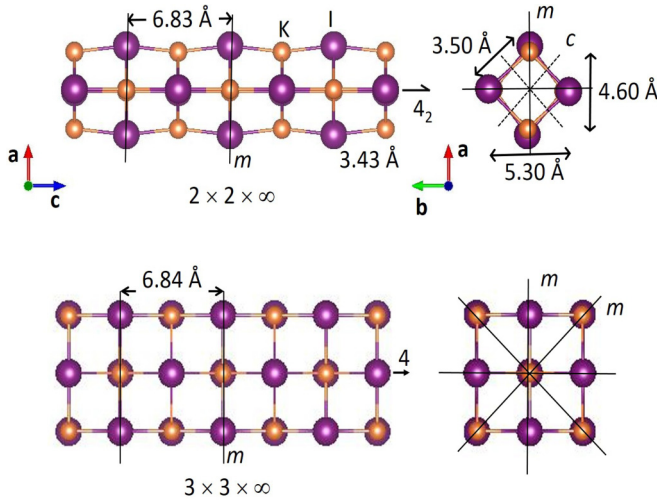


FIG. 1. Optimized equilibrium structure of freestanding  $2 \times 2$  and  $3 \times 3$  KI nanowires. Note that the color of potassium atoms (small orange circles) does not follow the standard CPK color scheme in order to discriminate them better from iodine atoms.

$3.532 \text{ \AA}$ . In what follows we will describe the  $3 \times 3$  nanowire in a coordinate system with the  $c$  axis along the 1D periodicity direction and  $a$  and  $b$  axes along the corresponding  $[100]$  and  $[010]$  bulk cubic directions. For the  $2 \times 2$  structure, however, we will define  $a$  and  $b$  as axes pointing along the  $45^\circ$  tilted directions  $[110]$  and  $[1\bar{1}0]$ , respectively. This choice allows for a simpler description of the normal modes of the  $2 \times 2$  nanowire because in this case the  $a$  and  $b$  axes lie in planes of proper mirror symmetry. In order to perform the calculations with a plane-wave (PW) basis set, periodic boundary conditions were imposed along the  $a$  and  $b$  axes with a period of  $20 \text{ \AA}$ . The geometry optimization of the nanowires converges to the structures shown in Fig. 1. The optimized nearest-neighbor K-I distances practically coincide for the two structures and are  $\approx 3.43 \text{ \AA}$  along the  $c$  axis and  $\approx 3.50 \text{ \AA}$  within the  $ab$  cross sections, respectively. The calculated contraction of the K-I distances along the nanowire axis is in good agreement with the previous HRTEM measurements [4] and theoretical models [8,14]. The main difference between the two types of nanowires is the considerable rhombic deformation of the cross section of the  $2 \times 2$  nanowire, which is elongated by  $\approx 0.35 \text{ \AA}$  along the I-I diagonals and contracted by the same amount along the K-K diagonals. At the same time, the rhombic deformation of the cross section of the  $3 \times 3$  structure is an order of magnitude smaller and consists of four almost perfect  $\text{K}_2\text{I}_2$  squares. All relevant interatomic distances for the two nanowires are shown in Fig. 1 and are listed in Table I for the  $2 \times 2$  nanowire and in Table S1 of the Supplemental Material [22] for the  $3 \times 3$  nanowire.

The symmetry elements for the two nanowires can be easily identified from Fig. 1. The set of symmetry generators of the  $2 \times 2$  nanowire consists of a fourfold screw axis  $4_2$  along  $c$ , mirror planes  $m$  parallel to the  $ab$ ,  $bc$ , and  $ac$  planes, and two gliding planes with  $1/2$  translation along  $c$ . Therefore, the  $2 \times 2$  structure can be described by the rod symmetry group  $p4_2/mmc$  (No. 41) with all atoms occupying 4d Wyckoff positions [23]. Similarly, the symmetry generators of the

TABLE I. Optimized interatomic distances for a freestanding  $2 \times 2$  KI nanowire.

Atomic pair	Distance ( $\text{\AA}$ )
Along $c$	
K-I	3.43297
K-K, I-I (the $c$ -period)	6.83128
In the $ab$ plane	
K-I	3.50662
K-K	4.60929
I-I	5.29815

$3 \times 3$  structure are a fourfold axis along  $c$ , three mirror planes  $m$  parallel to the  $ab$ ,  $bc$ , and  $ac$  planes, and two diagonal mirror planes normal to the  $a + b$  and  $a - b$  directions. Thus, the  $3 \times 3$  nanowire belongs to the rod group  $p4/mmm$  (No. 39) with K and I atoms occupying  $(1b, 4d, 4f)$  and  $(1a, 4g, 4c)$  Wyckoff positions, respectively [23].

## B. Normal modes

The normal modes were calculated for the optimized structures at four uniformly spaced points of the 1D Brillouin zone. A one-dimensional acoustic sum rule was imposed on the dynamical matrix at the  $\Gamma$  point in order to account for the four zero-frequency modes of a freely standing nanowire: the three free translations and the free rotation about the  $c$  axis. Since the unit cells of the  $2 \times 2$  and  $3 \times 3$  KI nanowires contain 8 and 18 atoms, respectively, their corresponding phonon spectra consist of 24 and 54 dispersion branches along the  $\Gamma$ -Z line. The phonon dispersion of the two nanowires was calculated by means of Fourier interpolation of the dynamical matrices obtained on the four-point grid. Figure 2 shows the dispersion curves for the  $2 \times 2$  and  $3 \times 3$  nanowires. No imaginary frequencies have been found so far, which proves the stability of the calculated equilibrium structures. The overall frequency dispersion along  $\Gamma$ -Z is very similar for the two systems with three groups of frequencies between 20 and 60, 70 and 110, and 130 and  $150 \text{ cm}^{-1}$  at  $q = 0$ , showing that, experimentally, it is difficult to separate the vibrational contributions of the  $2 \times 2$  and  $3 \times 3$  KI nanowires.

The normal modes of both nanowires at the  $\Gamma$  point are classified according to the irreducible representations of the  $4/mmm$  ( $D_{4h}$ ) point group. The symmetry decomposition was performed with the aid of SAM software available on the

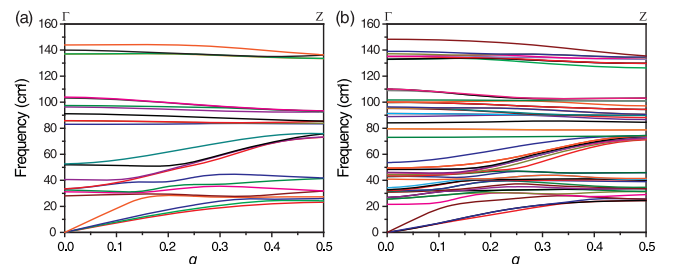


FIG. 2. Calculated phonon dispersion curves along the 1D Brillouin zone of (a) the  $2 \times 2$  KI nanowire and (b) the  $3 \times 3$  KI nanowire.

TABLE II. Calculated  $\Gamma$ -point frequencies (in  $\text{cm}^{-1}$ ) for the  $2 \times 2$  and  $3 \times 3$  KI nanowires.

$A_{1g}$	$A_{2g}$	$B_{1g}$	$B_{2g}$	$E_g$	$A_{2u}$	$B_{1u}$	$B_{2u}$	$E_u$
				$2 \times 2$				
			28	33				32
52		41					53	
	83							86
96		97	91					104
				137	135		140	
				$3 \times 3$				
			22	26				27
		31			33	34	31	32
41								43
46	43	45	46	49	54			48
		73						
84	89							80
								91
97		95						95
	102		100					100
			109	133	133	133		110
				135	136		137	
				139				

Bilbao Crystallographic Server [24]:

$$\Gamma_{22} = 2A_{1g} + 2A_{2g} + 2B_{1g} + 2B_{2g} + 2E_g + 2A_{2u} + 2B_{2u} + 4E_u \quad (1)$$

for the  $2 \times 2$  KI crystal, and

$$\Gamma_{33} = 4A_{1g} + 4A_{2g} + 4B_{1g} + 4B_{2g} + 4E_g + 6A_{2u} + 2B_{1u} + 2B_{2u} + 10E_u \quad (2)$$

for the  $3 \times 3$  KI crystal. The acoustic modes are  $A_{2u} + E_u$ . The zero-frequency rigid motions of the nanowires correspond to  $A_{2g}$  (rotation about  $c$ ),  $A_{2u}$  (translation along  $c$ ), and  $E_u$  (translation in the  $ab$  plane). The other  $A_{2g}$  and the two  $B_{2u}$  modes are optically silent. The remaining even ( $g$ ) modes are Raman active,

$$\Gamma_{22\text{Raman}} = 2A_{1g} + 2B_{1g} + 2B_{2g} + 2E_g, \quad (3)$$

$$\Gamma_{33\text{Raman}} = 4A_{1g} + 4B_{1g} + 4B_{2g} + 4E_g, \quad (4)$$

while the rest of the odd ( $u$ ) modes possess IR activity,

$$\Gamma_{22\text{IR}} = A_{2u} + 3E_u, \quad (5)$$

$$\Gamma_{33\text{IR}} = 5A_{2u} + 9E_u. \quad (6)$$

Therefore, accounting for the degeneracy of the  $E_g$  vibrations, 8 and 16 different frequencies can be expected in the Raman spectrum of the  $2 \times 2$  KI and  $3 \times 3$  KI nanowires, respectively. The calculated frequencies of the  $\Gamma$ -point modes are summarized in Table II.

In the two structures the  $A_{1g}$  and  $E_g$  vibrations involve similar types of atomic displacements. The totally symmetric  $A_g$  modes comprise radial-breathing-type motion of the K and I sublattices. The  $E_g$  modes involve atomic motions along the nanowire axis and could be characterized as shear-type

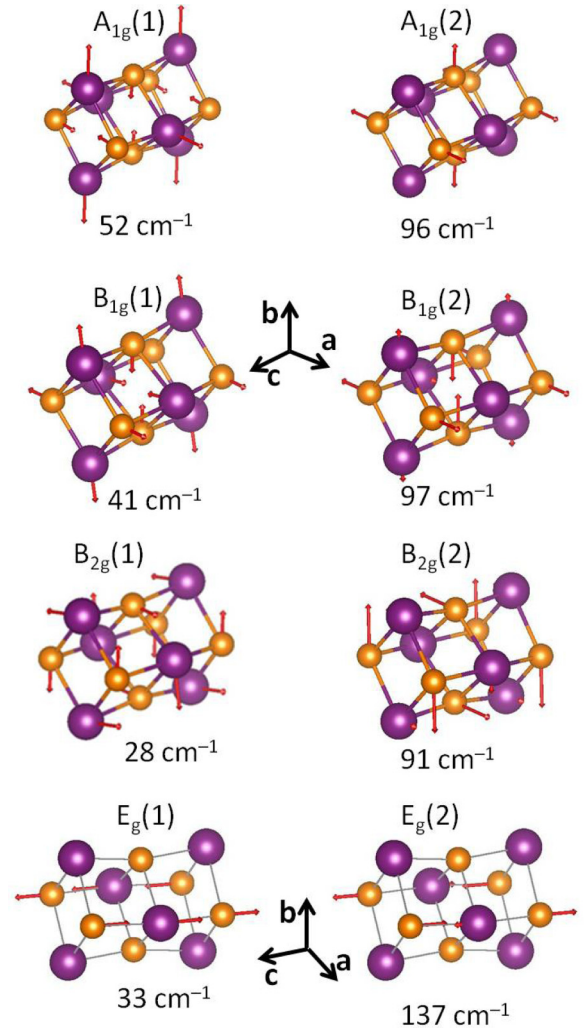


FIG. 3. Calculated atomic displacements for the Raman-active modes of a freestanding  $\text{K}_2\text{I}_2$  nanowire. Modes with the same symmetry are numbered in ascending order of their frequencies. Note that the color of potassium atoms (small orange circles) does not follow the standard CPK color scheme in order to discriminate them better from iodine atoms.

deformations of the two atomic sublattices. Figure 3 represents the corresponding calculated atomic displacements in the Raman-active vibrations for the  $2 \times 2$  nanowire. Modes with the same symmetry are numbered in ascending order of their frequencies. For the doubly degenerate  $E_g$  modes only one of the two independent components is shown for each frequency. The corresponding calculated Raman-active modes of the  $3 \times 3$  structure are shown in Fig. S2 of the Supplemental Material [22].

The  $B_{1g}$  modes of the  $2 \times 2$  nanowire can be considered counterparts of the corresponding  $A_{1g}$  modes, in which the alternating  $\text{K}_2\text{I}_2$  rhombuses vibrate out of phase, while the  $B_{2g}$  modes involve torsion-type deformations of the K and I sublattices. Due to the proper character of the fourfold axis in the  $3 \times 3$  nanowire, the  $B_{1g}$  and  $B_{2g}$  modes in this structure involve antiphase radial motions of the symmetry-related atoms within the same  $\text{K}_5\text{I}_4/\text{K}_4\text{I}_5$  plane.

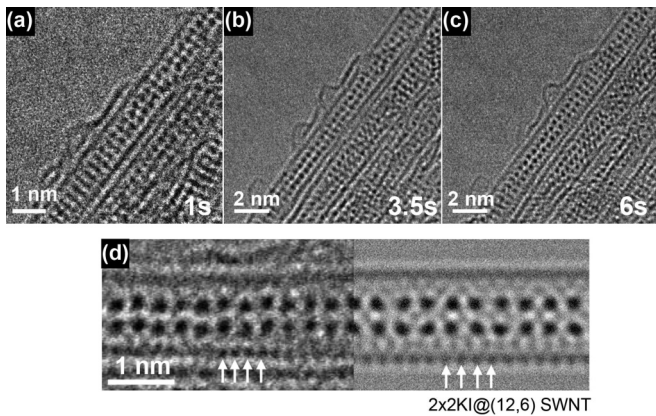


FIG. 4. (a) Time-lapse high-resolution plan-view image of a bundle of NI96 SWCNTs filled with KI, showing one SWCNT filled with  $(2 \times 2)$ KI crystal and another one just beside it filled with a  $(3 \times 3)$ KI crystal. (b) and (c) Other plan-view images at slightly lower magnifications showing SWCNT bundles with a high filling fraction. (d) Close-up of an individual SWCNT [from (c)] filled with  $(2 \times 2)$ KI, in which the nanotube walls are clearly visible, indicating that the nanotube is chiral and tilted. To the right is an image simulation, made using a standard multislice protocol, of a  $(2 \times 2)$ KI crystal in a  $(12,6)$  conformation SWCNT tilted out of plane by  $10^\circ$ .

#### IV. EXPERIMENTAL RESULTS AND DISCUSSION

In this section, we first compare the experimental geometry of KI filled nanotubes observed using HRTEM with the relaxed structures of the KI nanowires obtained with *ab initio* calculations. Afterwards, we describe the Raman experiments performed on the same composite systems imaged with TEM. We first point out that new Raman modes occur in the spectral RBM region of the encapsulating CNTs. These modes are ascribed to specific vibrations of the embedded 1D KI crystals. Close inspection of the calculated phonons of the stand-alone 1D KI crystals shows good correspondence with the additional Raman lines appearing in the real systems.

##### A. Electron microscopy

All nanotube samples were first characterized by HRTEM. Observation of the pristine, unfilled SWCNTs indicated that more than 90% of them in both the NI96 and NI99 samples had a mean diameter in the range of 1.2–1.6 nm, with the remaining tubes deviating typically only by a maximum of 0.5 nm from this range. Images taken after treating SWCNTs with KI evidenced a high fraction of successful KI encapsulation for composite KI@SWCNTs samples, with very clear crystalline structure inside the tubes. Both  $2 \times 2$  and  $3 \times 3$  KI fillings were observed (Figs. 4(a)–4(c) and Fig. S1 [22]). The quality of the images is considerably improved in comparison to previous publications [4] with well-resolved crystals, consisting of a succession of  $K_2I_2$  and  $K_5I_4/K_4I_5$  planes along the tube axis for the  $2 \times 2$  and  $3 \times 3$  fillings, respectively. The interplane distance is  $\approx 0.35$  nm for both fillings, which deviates from the calculated value by only 2%. The observed in-plane K-I distance of  $\approx 0.4$  nm in the  $2 \times 2$  nanowire, however, is superior to the calculated distance in a

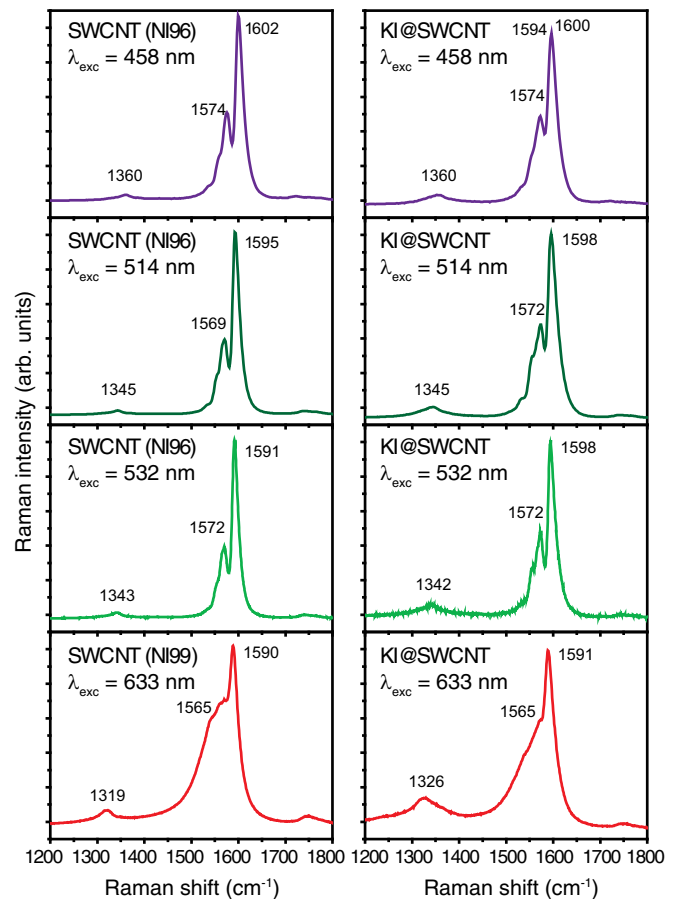


FIG. 5. Experimental Raman spectra of ultrapure-grade SWCNT (left panels) and composite (right panels) KI@SWCNT samples recorded in the  $G$ -mode region at different laser excitations. Frequencies of Lorentzian components are indicated for  $G^-$  and  $G^+$  bands.

freely standing crystal by 0.05 nm ( $0.5 \text{ \AA}$ ). As discussed in the literature [8,25], the lateral expansion of the encapsulated nanowire is most likely an electrostatic effect arising from the charge transfer between the iodine anions and the nanotube wall.

##### B. High-frequency Raman spectra

The expected eigenfrequencies of the KI nanowires are predicted in the spectral range below the characteristic RBM frequencies of the enclosing SWCNTs. However, it is instructive to inspect the spectral range above  $1000 \text{ cm}^{-1}$  in order to compare the behavior of the tangential nanotube modes upon KI encapsulation with the data already reported in the literature for other similar systems. Figure 5 displays the Raman spectra of pristine and hybrid SWCNT for the  $D$ - and  $G$ -mode spectral regions. In the pristine tubes these modes are located at  $\nu_D = 1360$ ,  $\nu_{G^-} = 1574$ ,  $\nu_{G^+} = 1602$ , and  $\nu_{G'}$  =  $2709 \text{ cm}^{-1}$  for the laser excitation with  $\lambda_{\text{exc}} = 458$ . At  $\lambda_{\text{exc}} = 514$  nm, the mode frequencies shift to 1345, 1569, 1595  $\text{cm}^{-1}$ , and 2679  $\text{cm}^{-1}$ , respectively. In KI@SWCNT samples, there is a slight upshift of the main  $G^-$  and  $G^+$  lines towards 1572 and 1598  $\text{cm}^{-1}$  for  $\lambda_{\text{exc}} = 514$  nm and a larger upshift for the  $G^+$  line at  $\lambda_{\text{exc}} = 532$  nm ( $+7 \text{ cm}^{-1}$ ). It can be noticed that

the intensity ratio of the  $G^+$  mode to the  $G^-$  mode decreases in KI@SWCNT, indicating that the tubes with the smallest diameters are mostly filled by KI. For  $\lambda_{\text{exc}} = 633$  nm, the NI96 and NI99 ultrapure samples yield very similar Raman spectra with a  $G$  feature presenting a Breit-Wigner-Fano line shape region typical of metallic SWCNT, where the  $G$  band exhibits a low-frequency side forming a tail extending down to  $1400\text{ cm}^{-1}$  with several unresolved vibrational components [26]. In the metallic NI96 pure tubes, the Raman bands appear at lower frequency ( $1314$ ,  $1559$ ,  $1584$ , and  $2612\text{ cm}^{-1}$ ) than for other excitations, while in the metallic NI96 composite, the frequency of these modes is strongly upshifted at  $1326$ ,  $1570$ ,  $1596$ , and  $2636\text{ cm}^{-1}$  with respect to the pristine ones. The disorder-induced modes  $D$  and  $G'$  are very sensitive to the encapsulation of the crystals [27]. In composite, the  $D$  mode is enhanced in intensity for all laser excitations, and the  $G'$  line (not shown here) is strongly reduced in intensity for  $\lambda_{\text{exc}} = 458$  and  $633$  nm. The C-C bond length change upon encapsulation is related to the frequency shift (stiffening) observed by  $-\Delta r_{\text{C-C}}/r_{\text{C-C}} = \Delta\omega/\omega$ , where  $r_{\text{C-C}}$  is the C-C bond length and  $\omega$  is the frequency, which for an excitation of  $633$  nm gives a bond length variation of  $-0.4\%$ . This result agrees with similar upshifts found upon  $\text{MnTe}_2$  encapsulation in SWCNTs [27]. As speculated in Ref. [8], the frequency upshift of the SWCNT tangential modes could also be a result

of an electronic transfer from the embedded KI nanowire to the carbon atoms.

### C. Low-frequency Raman spectra

Figure 6 displays the low-frequency Raman spectra of pristine and composite SWCNTs taken for several laser excitations. The spectra of pristine and composite SWCNTs exhibit RBM vibrations whose vibrational components are listed in Table III. The diameters of the nanotubes revealing these modes can be deduced easily by applying the empirical relationship  $\nu\text{ (cm}^{-1}\text{)} = 223.8/d\text{ (nm)}$  [28]. We have inserted these diameter values in the Kataura plot of Levshov *et al.* [29] at the exciting energies used in the Raman experiments. The corresponding data points overlie the  $M_{11}$ ,  $S_{33}$ , and  $S_{44}$  branches of the Kataura plot, but the exact chiralities of the nanotubes cannot be determined unequivocally. Our data suggest that NI96/NI99 samples have metallic nanotubes with four diameters,  $1.12$ ,  $1.29$ ,  $1.33$  and  $1.47$  nm, which resonate in the red part of the photon spectrum, as well as a variety of semiconducting nanotubes with diameters between  $1.22$  and  $1.60$  nm resonating for higher photon energies. According to Scaets *et al.* [14], the molecular and electronic structures of the ionic intercalate in KI@SWCNT composites depend primarily on the CNT diameter and are almost insensitive to the conductivity and the geometry (chirality) of the nanotube. Therefore, the lack of information for the exact CNT chiralities is not crucial for the interpretation of the experimental Raman data.

The overall intensity of the nanotube RBM band drops at an absolute scale for all excitation wavelengths. This fact could be explained by a charge transfer between KI and

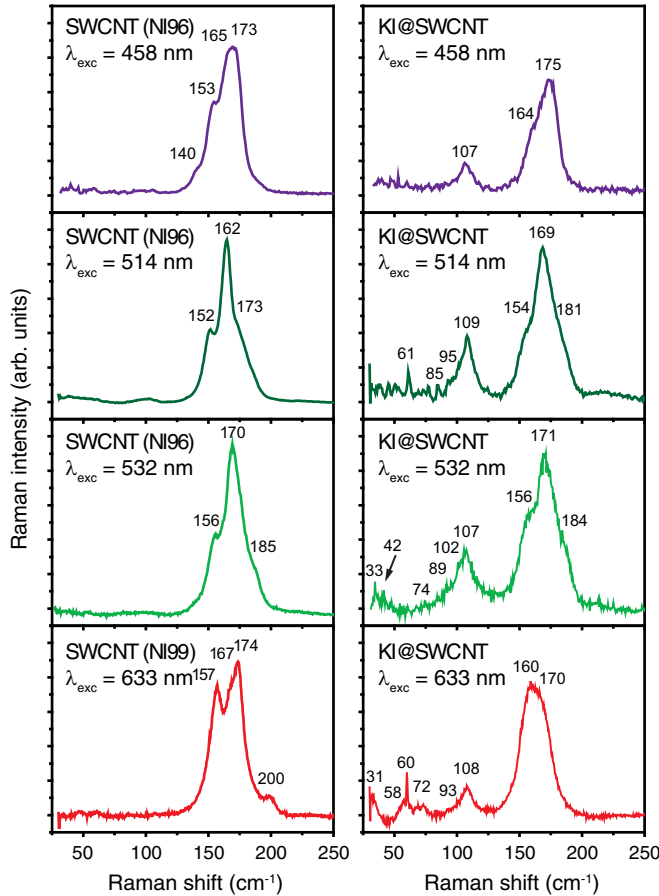


FIG. 6. Experimental Raman spectra of ultrapure-grade SWCNT (left panels) and composite (right panels) KI@SWCNT samples recorded in the RBM-mode region at different laser excitations.

TABLE III. Experimental Lorentzian component frequencies of radial breathing modes obtained for the NI96 and NI99 (denoted by an asterisk) ultrapure nanotubes vs SWCNT diameter and exciting laser energies. The metallic (M) and semiconducting (SC) SWCNTs associated with these diameters are deduced from the Kataura plot of Levshov *et al.* [29].

$\lambda_{\text{exc}}$ (nm)	$E$ (eV)	$\nu$ ( $\text{cm}^{-1}$ )	$d$ (nm) = $223.8/\nu$	Type
458	2.71	140	1.60	SC
458	2.71	153	1.46	SC
458	2.71	165	1.36	SC
458	2.71	173	1.29	SC
514	2.42	148	1.51	SC
514	2.42	152	1.47	SC
514	2.42	162	1.38	SC
514	2.42	173	1.29	SC
514	2.42	183	1.22	SC
532	2.34	155	1.44	SC
532	2.34	170	1.32	SC
532	2.34	185	1.21	SC
633	1.96	152	1.47	M
633	1.96	168	1.33	M
633	1.96	157	1.42	M*
633	1.96	167	1.34	M*
633	1.96	174	1.29	M*
633	1.96	200	1.12	M*

TABLE IV. Closest matches between the frequencies  $\omega_{\text{exp}}$  of the experimentally observed new Raman lines and the DFT predictions for freely standing KI nanowires.

$\omega_{\text{exp}}$ (cm <sup>-1</sup> )	$2 \times 2$ KI	$3 \times 3$ KI
34	$E_g$	$B_{1g}$
41	$B_{1g}$	$A_{1g}$
60	$A_{1g}$	
73		$B_{1g}$
108	$A_{1g}$ and/or $B_{1g}$	$A_{1g}$ and/or $B_{1g}$ and/or $B_{2g}$

SWCNT [17], which changes the electronic density around the Van Hove singularities of SWCNTs and the Raman scattering resonant conditions thereof. A systematic shift of the RBM frequencies by  $1\text{--}4\text{ cm}^{-1}$  towards higher wave numbers was also established in KI@SWCNT composites and will be discussed later. The exact value of the frequency shift for a given RBM component, however, varies among different measurement spots, which could be related to fluctuation of the fraction of filled CNTs in different parts of the sample.

For all laser excitation energies the filled samples display a relatively broad and intense additional Raman band spread between  $\approx 90$  and  $120\text{ cm}^{-1}$  with a maximum at  $106\text{--}108\text{ cm}^{-1}$ . This band is associated, depending on the excitation used, with other narrower and less intense lines at  $\approx 34, 41, 57$  (shoulder at  $633\text{ nm}$ ),  $60$ , and  $73\text{ cm}^{-1}$ . Both filled samples (NI96 and NI99) exhibit the same novel lines, while they are completely absent in the pristine nanotubes. We therefore ascribe these experimental signals to the embedded KI crystals inside the SWCNTs in the composite samples. In Table IV the frequencies of the additional lines are tentatively matched to the DFT-calculated vibrational modes (see Table II) for the  $2 \times 2$  and  $3 \times 3$  KI nanowires. We also note that for several  $\lambda_{\text{exc}}$ , the highest RBM frequency line drops in intensity with respect to its counterpart in the pristine samples (Fig. 6). This indicates that SWCNTs with a smaller diameter are preferentially filled by KI, which is consistent with HRTEM observations. This fact also suggests that the strong line at  $60\text{ cm}^{-1}$  and, to a large extent, the band at  $108\text{ cm}^{-1}$  are associated with the  $2 \times 2$  KI nanowires, which fit into the smaller-diameter nanotubes. The band at  $108\text{ cm}^{-1}$  is considerably larger than the other new spectral features. Two poorly resolved shoulders of its spectral maximum are seen at  $\approx 93$  and  $100\text{ cm}^{-1}$ , which indicate a possible convolution of several overlapping lines corresponding to a variety of radial modes in both fillings:  $A_{1g}$  and  $B_{1g}$  for the  $2 \times 2$  nanowire and  $A_{1g}$ ,  $B_{1g}$ , and  $B_{2g}$  for the  $3 \times 3$  structure. This assignment corroborates the fact that the strongest Raman lines observed in HgTe@SWCNT composites have been assigned to the radial  $A_{1g}$  and  $B_{1g}$  modes of the encapsulated  $2 \times 2$  HgTe nanowires [19]. In the case of a HgTe nanowire these modes resonate at an excitation energy of  $1.76\text{ eV}$ , which corresponds to an intrawire electronic transition. In our case, however, the estimated electronic gap of the KI nanowires is greater than  $4\text{ eV}$ ; thus, no resonance in the visible range is expected, which corroborates the nonresonant behavior of the  $108\text{-cm}^{-1}$  band.

## V. IMPLICATIONS FOR THE NANOWIRE-NANOTUBE INTERACTION

In this section we carry out a detailed perturbative analysis of the theoretical and experimental frequencies which, combined with the structural results, gives evidence for conspicuous nanowire-CNT interactions.

While the lines at  $34, 41$ , and  $73\text{ cm}^{-1}$  correspond very well to the theoretically calculated frequencies, those at  $60$  and  $108\text{ cm}^{-1}$  are systematically upshifted by  $8$  and  $12\text{ cm}^{-1}$ , respectively, with respect to the suggested calculated counterparts. The positive frequency shift  $\Delta\omega \approx 12\text{ cm}^{-1}$  of the K breathing mode is consistent with an increase in the force constant associated with the potassium radial motion by  $\Delta f_K \approx 2M_K\omega\Delta\omega = 0.33\text{ eV/\AA}^2$ , where  $M_K = 39\text{ a.u.}$  is the atomic mass of potassium and  $\omega = 96\text{ cm}^{-1}$  is the unperturbed frequency of the K mode for the freely standing nanowire. For the iodine radial motion a similar value  $\Delta f_I = 0.43\text{ eV/\AA}^2$  can be estimated by using  $M_I = 140\text{ a.u.}$ ,  $\omega = 52\text{ cm}^{-1}$  (the calculated frequency for the I breathing mode), and  $\Delta\omega = 8\text{ cm}^{-1}$ . The modification of the force constant for the radial K (I) motion can be represented as  $\Delta f_{K(I)} = \Delta f_{K(I)}^{\text{int}} + \Delta f_{K(I)}^{\text{ext}}$ . The first term corresponds to the “internal” interactions between the ions within the KI nanowire. The second one arises from “external” interactions between the ions of the nanowire and the carbon atoms in the CNT wall.

The internal contribution to the force constants is due to the elongation of the in-plane K-I bonds upon encapsulation, as well as to additional Coulombic interactions due to the charge transfer between the KI nanowire and the surrounding SWCNT. The elongation of the bonds normally tends to soften the phonon frequencies. As rationalized in Ref. [8], the presence of additional electrostatic repulsion between the bonded atoms, however, may result in an overall increase in the effective force constants. These arguments apply to the nearly planar hexagonal arrangement of the carbon atoms on the SWCNT wall and provide an explanation for the  $G^+$ - and  $G^-$ -mode hardening upon KI encapsulation. However, the case of a KI nanowire deserves special consideration since K and I ions are situated in a low-symmetry nonplanar environment. That is why we will make a model estimate of the electrostatic contribution to the force constants describing the radial potassium and iodine motion. According to Ref. [8], on average  $0.28$  of an electron is transferred from the iodine anion to the nanotube. This is equivalent to pinning an additional charge of  $q = +0.28$  on each anion site. The interaction between the added charges and the potassium cations may affect the frequency of the K radial motion. The force constant corresponding to the electrostatic interaction between two charges falls off with the distance  $r$  as  $1/r^3$ . Therefore, for the sake of a semiquantitative estimate, it is sufficient to consider the interaction of a given K cation with the added charges on only the nearest-neighbor anions, as shown in Fig. 7(a). According to the HRTEM results, the intraplane and interplane K-I distances are  $a \approx 4.0\text{ \AA}$  and  $b = c/2 \approx 3.5\text{ \AA}$ , respectively (in the notation of Ref. [8]). By assuming a  $+1$  charge on K, it is straightforward to derive that the additional Coulombic force constant for the pure K radial motion is given by

$$\Delta f_K^{\text{int}} = (14.4\text{ eV \AA})q(0.5/a^3 - 2/b^3). \quad (7)$$

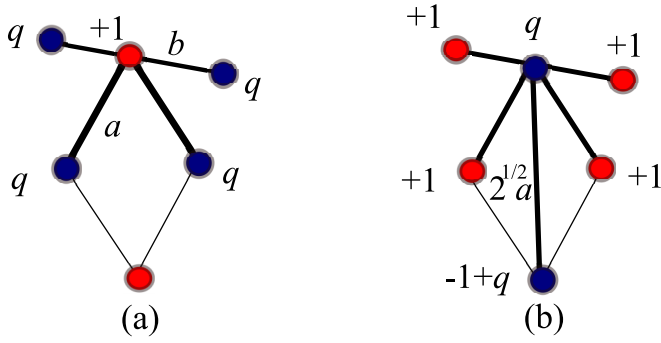


FIG. 7. Nearest-neighbor electrostatic interactions (thick lines) perturbing the radial force constant for (a) potassium and (b) iodine. The potassium and iodine ions are represented as red and blue circles, respectively.

For  $q = +0.28$  we obtain  $\Delta f_K^{\text{int}} \approx -0.16 \text{ eV}/\text{\AA}^2$ . Surprisingly, the Coulombic interactions tend to soften the frequency of the radial K motion by  $\Delta\omega = -6 \text{ cm}^{-1}$  with respect to the freely standing nanowire. As evident from Eq. (7), the negative force constant arises from the electrostatic repulsion between the K cation and the positive charges added on the I anions of the same atomic row. It is easy to deduce [see Fig. 7(b)] that the corresponding Coulombic correction to the I radial force constant is

$$\Delta f_I^{\text{int}} = \Delta f_K^{\text{int}} - (14.4 \text{ eV } \text{\AA})2^{3/2}(1 - q/2)q/a^3. \quad (8)$$

The first term describes the interaction of the added positive charge  $q$  on a given iodine anion with the positive  $+1$  charges of the surrounding potassium cations. The second term corresponds to the additional electrostatic interaction between the two iodine anions situated on the I-I diagonal of the  $\text{K}_2\text{I}_2$  plane. Both terms are negative and give  $\Delta f_I^{\text{int}} \approx -0.30 \text{ eV}/\text{\AA}^2$  and, correspondingly,  $\Delta\omega = -11 \text{ cm}^{-1}$  for the I breathing mode.

The above estimates provide evidence that the intrawire interactions fail to explain the frequency shift of the radial nanowire modes upon encapsulation in the SWCNT. Therefore, we should admit that the positive frequency shift of these vibrations is due to the interactions between the nanowire and the surrounding nanotube. On the basis of the deduced values of  $\Delta f_{K(I)}$  and  $\Delta f_{K(I)}^{\text{int}}$ , one may conclude that the observed frequencies of the radial breathing modes of the nanowire are consistent with “external” force constants  $\Delta f_K^{\text{ext}} \approx 0.56 \text{ eV}/\text{\AA}^2$  and  $\Delta f_I^{\text{ext}} \approx 0.73 \text{ eV}/\text{\AA}^2$ . These values coerce the contributions of several interactions, such as dispersive van der Waals [2–5], direct electrostatic (monopole or multipole), induced dipole, and exchange-correlation contributions arising from the electron density overlap between the ions of the nanowire and the carbon atoms in the nanotube [8]. In this respect the greater value of the radial force constant for iodine is consistent with the fact that the iodine anion has a larger radius than the potassium cation and, therefore, its electron density overlaps more strongly with the electron density of the carbon atoms.

The nanowire-nanotube interaction also has another spectroscopically observable effect. Since the  $A_{1g}$  radial nanowire modes are totally symmetric, they can mix dynamically with the nanotube RBM mode. It is straightforward to derive that

the nanotube-nanowire interaction shifts the frequency of the RBM by

$$\Delta\omega_{\text{RBM}} \approx (\Delta f_K^{\text{ext}} + \Delta f_I^{\text{ext}})/(2nM_C\omega_{\text{RBM}}), \quad (9)$$

where  $\omega_{\text{RBM}}$  is the unperturbed RBM frequency (empty SWCNT),  $M_C$  is the mass of the carbon atom, and  $n$  is the number of carbon atoms per KI formula unit. For a 1.35-nm SWCNT, we have  $\omega_{\text{RBM}} \approx 165 \text{ cm}^{-1}$ . A value of  $n$  can be deduced by considering, for example, a fragment of a (10,10) SWCNT with a length of  $\approx 7 \text{ \AA}$  corresponding to the periodicity of the nanowire (see Fig. S3 of the Supplemental Material [22]). Such a fragment contains 120 carbon atoms, which gives  $n \approx 30$  since the unit cell of the nanowire contains four formula units. Thus, the expected frequency shift upon KI crystal encapsulation is  $\Delta\omega_{\text{RBM}} \approx +2.9 \text{ cm}^{-1}$ . This value is the same order of magnitude as the experimentally observed RBM frequency shifts in the KI@SWCNT samples.

## VI. CONCLUSION

In this work we reported an *ab initio* analysis of the vibrational dynamics of stand-alone  $2 \times 2$  and  $3 \times 3$  one-dimensional KI crystals, supported by HRTEM imaging and Raman scattering experiments. The DFT calculations predict stable ground states for the two EN types. Interestingly, the experimentally TEM measured in-plane K-I distances of  $2 \times 2$  KI crystals embedded in small-diameter CNTs surpass the calculated values for a freely standing 1D crystal by  $\approx 0.5 \text{ \AA}$ . This geometric effect evidences an electron transfer from the KI crystal to the surrounding CNT. Charge transfer is also supported by the experimentally established slight hardening of the tangential SWCNT Raman modes upon KI encapsulation.

We presented concomitantly a direct spectroscopic observation of additional modes ascribed to Raman lines of CNT-encapsulated  $2 \times 2$  and  $3 \times 3$  KI nanowires. These vibrational lines do not show any resonance effect with laser excitation, in sharp contrast to HgTe Raman lines in SWCNTs. Thus, the embedded KI nanowire preserves the UV optical absorption edge of the bulk KI, in contrast to the telluride and selenide ENs.

Good correspondence was obtained between the calculated frequencies of the tangential KI nanowire modes and the observed additional frequencies of the KI@SWCNT samples. However, the radial modes of the KI nanowires are systematically upshifted with respect to the theoretical predictions. This deviation is treated by a perturbative analysis which demonstrates that the excess radial restoring force is not of electrostatic origin but stems from nanowire-CNT interactions. Moreover, we estimated the strength of the radial force constant for K-CNT and I-CNT interactions, which is not yet documented. It turns out that these force constants are much weaker than those expected for covalent bonding of the nanowire to the CNT. Also, the fact that the interaction is of radial character excludes a nanowire-CNT functionalization because in that case the bond-bending forces would harden the frequencies of the tangential modes as well. Thus, we come to the conclusion that the K-CNT and I-CNT interactions are primarily of van der Waals character.

Finally, the present study as a whole confirms the relevance of Raman spectroscopy in the low-frequency domain as a



direct characterization tool for probing the dynamical properties of embedded or confined nanowires with ionic bonding.

### ACKNOWLEDGMENTS

This work was supported by the French-Bulgarian bilateral program PHC RILA through Grants No. DHTC-France 01/10/09.05.2017 and No. 38661ZF and by Contract

No. 80 10-9/12.04.2017 of the Scientific Fund of Sofia University. N.K. participated in this project during a stay at IMN. The authors thank Harrison Trehwitt for assistance with sample preparation. E.F. thanks Warwick University for the hospitality during the synthesis of the materials. J.S. is indebted for support to the EPSRC from Grants No. EP/M010643/1 and No. EP/R019428/1. V.G.I. also acknowledges partial support from Contract No. FNI-TO2/26 of the Bulgarian National Scientific Fund.

- 
- [1] A. A. Eliseev, N. I. Verbitskiy, A. A. Volykhov, A. V. Fedorov, O. Y. Vilkov, I. I. Verbitskiy, M. M. Brzhezinskaya, N. A. Kiselev, and L. V. Yashina, *Carbon* **99**, 619 (2016).
- [2] J. Sloan, J. Hammer, M. Zwiefka-Sibley, M. L. H. Green, and J. Sloan, *Chem. Commun.* **0**, 347 (1998).
- [3] R. R. Meyer, J. Sloan, R. E. Dunin-Borkowski, A. I. Kirkland, M. C. Novotny, S. R. Bailey, J. L. Hutchison, and M. L. H. Green, *Science* **289**, 1324 (2000).
- [4] J. Sloan, M. Novotny, S. Bailey, G. Brown, C. Xu, V. Williams, S. Friedrichs, E. Flahaut, R. Callender, A. York, K. Coleman, M. Green, R. Dunin-Borkowski, and J. Hutchison, *Chem. Phys. Lett.* **329**, 61 (2000).
- [5] J. Sloan, A. I. Kirkland, J. L. Hutchison, and M. L. H. Green, *C. R. Phys.* **4**, 1063 (2003).
- [6] M. M. Rahman, M. Kisaku, T. Kishi, T. A. Roman, W. A. Diño, H. Nakanishi, and H. Kasai, *J. Phys. Soc. Jpn.* **74**, 742 (2005).
- [7] M. Weissmann, G. García, M. Kiwi, R. Ramírez, and C.-C. Fu, *Phys. Rev. B* **73**, 125435 (2006).
- [8] E. Bichoutskaia and N. C. Pyper, *J. Chem. Phys.* **137**, 184104 (2012).
- [9] R. Carter, J. Sloan, A. I. Kirkland, R. R. Meyer, P. J. D. Lindan, G. Lin, M. L. H. Green, A. Vlandas, J. L. Hutchison, and J. Harding, *Phys. Rev. Lett.* **96**, 215501 (2006).
- [10] L. V. Yashina, A. A. Eliseev, M. V. Kharlamova, A. A. Volykhov, A. V. Egorov, S. V. Savilov, A. V. Lukashin, R. Püttner, and A. I. Belogorokhov, *J. Phys. Chem. C* **115**, 3578 (2011).
- [11] T. Fujimori, A. Morelos-Gómez, Z. Zhu, H. Muramatsu, R. Futamura, K. Urita, M. Terrones, T. Hayashi, M. Endo, S. Y. Hong, Y. C. Choi, D. Tománek, and K. Kaneko, *Nat. Commun.* **4**, 2162 (2013).
- [12] R. Senga, H.-P. Komsa, Z. Liu, K. Hirose-Takai, and A. V. K. K. Suenaga, *Nat. Mater.* **13**, 1050 (2014).
- [13] H.-P. Komsa, R. Senga, K. Suenaga, and A. V. Krasheninnikov, *Nano Lett.* **17**, 3694 (2017).
- [14] E. L. Sceats, J. C. Green, and S. Reich, *Phys. Rev. B* **73**, 125441 (2006).
- [15] P. V. C. Medeiros, S. Marks, J. M. Wynn, A. Vasylenko, Q. M. Ramasse, D. Quigley, J. Sloan, and A. J. Morris, *ACS Nano* **11**, 6178 (2017).
- [16] A. Vasylenko, S. Marks, J. M. Wynn, P. V. C. Medeiros, Q. M. Ramasse, A. J. Morris, J. Sloan, and D. Quigley, *ACS Nano* **12**, 6023 (2018).
- [17] A. Ilie, J. S. Bendall, D. Roy, E. Philp, and M. L. H. Green, *J. Phys. Chem. B* **110**, 13848 (2006).
- [18] M. Sendova, E. Flahaut, and T. Hartsfield, *J. Appl. Phys.* **108**, 044309 (2010).
- [19] J. H. Spencer, J. M. Nesbitt, H. Trehwitt, R. J. Kashtiban, G. Bell, V. G. Ivanov, E. Faulques, J. Sloan, and D. C. Smith, *ACS Nano* **8**, 9044 (2014).
- [20] P. Giannozzi, S. Baroni, N. Bonini, M. Calandra, R. Car, C. Cavazzoni, D. Ceresoli, G. L. Chiarotti, M. Cococcioni, I. Dabo, A. D. Corso, S. de Gironcoli, S. Fabris, G. Fratesi, R. Gebauer, U. Gerstmann, C. Gougoussis, A. Kokalj, M. Lazzeri, L. Martin-Samos, N. Marzari, F. Mauri, R. Mazzarello, S. Paolini, A. Pasquarello, L. Paulatto, C. Sbraccia, S. Scandolo, G. Sclauzero, A. P. Seitsonen, A. Smogunov, P. Umari, and R. M. Wentzcovitch, *J. Phys.: Condens. Matter* **21**, 395502 (2009).
- [21] J. P. Perdew, K. Burke, and M. Ernzerhof, *Phys. Rev. Lett.* **77**, 3865 (1996).
- [22] See Supplemental Material at <http://link.aps.org/supplemental/10.1103/PhysRevB.98.125429> for HRTEM images of filled SWCNTs, the calculated equilibrium parameters and  $\Gamma$ -point normal modes of stand-alone  $3 \times 3$  KI nanowires.
- [23] *International Tables of Crystallography Volume E: Subperiodic Groups* (Wiley, Hoboken, NJ, 2010).
- [24] E. Kroumova, M. I. Aroyo, J. M. Perez-Mato, A. Kirov, C. Capillas, S. Ivantchev, and H. Wondratschek, *Phase Transitions* **76**, 155 (2003).
- [25] E. Bichoutskaia and N. C. Pyper, *J. Phys. Chem. B* **110**, 5936 (2006).
- [26] S. D. M. Brown, A. Jorio, P. Corio, M. S. Dresselhaus, G. Dresselhaus, R. Saito, and K. Kneipp, *Phys. Rev. B* **63**, 155414 (2001).
- [27] L.-J. Li, T.-W. Lin, J. Doig, I. B. Mortimer, J. G. Wiltshire, R. A. Taylor, J. Sloan, M. L. H. Green, and R. J. Nicholas, *Phys. Rev. B* **74**, 245418 (2006).
- [28] S. Lefrant, *Current Appl. Phys.* **2**, 479 (2002).
- [29] D. Levshov, H. Tran, M. Paillet, R. Arenal, X. Than, A. Zahab, Y. Yuzyuk, J.-L. Sauvajol, and T. Michel, *Carbon* **114**, 141 (2017).